Hindawi Publishing Corporation
International Journal of Geophysics
Volume 2011, Article ID 805059, 12 pages
doi:10.1155/2011/805059

Research Article

2D Model Study of CO_2 Plumes in Saline Reservoirs by Borehole Resistivity Tomography

Said A. al Hagrey

Department of Geophysics, University of Kiel, Otto-Hahn-Platz 1, 24118 Kiel, Germany

Correspondence should be addressed to Said A. al Hagrey, sattia@geophysik.uni-kiel.de

Received 1 February 2011; Revised 7 September 2011; Accepted 14 September 2011

Academic Editor: Michael S. Zhdanov

The performance of electrical resistivity tomography (ERT) in boreholes is studied numerically regarding changes induced by CO_2 sequestration in deep saline reservoirs. The new optimization approach is applied to generate an optimized data set of only 4% of the comprehensive set but of almost similar best possible resolution. Diverse electrode configurations (mainly tripotential α and β) are investigated with current flows and potential measurements in different directions. An extensive 2.5D modeling (>100,000 models) is conducted systematically as a function of multiparameters related to hydrogeology, CO_2 plume, data acquisition and methodology. ERT techniques generally are capable to resolve storage targets (CO_2 plume, saline host reservoir, and impermeable cap rock), however with the common smearing effects and artefacts. Reconstructed tomograms show that the optimized and multiply oriented configurations have a better-spatial resolution than the lateral arrays with splitting of potential and current electrode pairs between boreholes. The later arrays are also more susceptible to telluric noise but have a lower level of measurement errors. The resolution advance of optimized and multiply oriented configurations is confirmed by lower values for ROI (region of index) and residual (relative model difference). The technique acceptably resolves targets with an aspect ratio down to 0.5.

1. Introduction

The need to manage the global CO_2 emissions for mitigating the greenhouse effect has led to a world wide research to reduce atmospheric CO_2. Techniques of carbon capture and storage (CCS) must (1) be effective and cost-competitive, (2) provide stable, long-term storage, and (3) be environmentally benign. Potential terrestrial media for CO_2 storage include depleted oil and gas reservoirs, unmineable coal seams, and deep saline water reservoirs capped by impermeable rock to prevent upward leakage.

CO_2 exists in the gas phase at standard atmospheric temperature and pressure. Above the dynamic critical point (>31.1°C, >7.38 MP, density >0.469 g/cm^3), CO_2 changes to a supercritical fluid phase; it diffuses through solids like a gas and dissolves material like a liquid. CO_2 has long been injected in the subsurface to enhance oil, gas, and coalbed methane recovery and storage. This injection has been mainly monitored using seismic time-lapse imaging (e.g., Sleipner oil field in North Sea, e.g., [1]). However, investigations on brine-saturated sandstones showed that the electrical resistivity (ρ) is more sensitive to CO_2 saturation than is seismic velocity (Figure 1). This may justify application of electrical resistivity tomography (ERT), particularly in boreholes, for monitoring resistive supercritical CO_2 plumes in a deep saline reservoir (e.g., [2]). This reservoir formation normally consists of a highly resistive matrix (e.g., sandstone and limestone) and a conductive pore brine. Here, CO_2 saturation can be predicted using the law of Archie [3]:

$$\rho = a\rho_w \Phi^{-m} S_w^{-n'}, \tag{1}$$

$$\rho_{CO_2} = a\rho_w \Phi^{-m} \left(1 - S_{CO_2}\right)^{-n'}, \tag{2}$$

where ρ, ρ_w, ρ_{CO_2} = bulk, fluid, and CO_2 resistivity, respectively, Φ = porosity, S_w, S_{CO_2} = water, and CO_2 saturation, a, m, n' = constants.

Recent developments have enabled installing deep boreholes with coated (insulating) casing and fixed electrode arrays for ERT monitoring (e.g., [5]). Forward modeling and inversion algorithms have also been developed for better monitoring CO_2 plume scenarios in deep saline reservoirs and coal seams (e.g., [6, 7]). In 2008 we started the interdisciplinary project "CO_2 MoPa" (modeling and parameterization of CO_2 storage in deep saline formations for dimensions

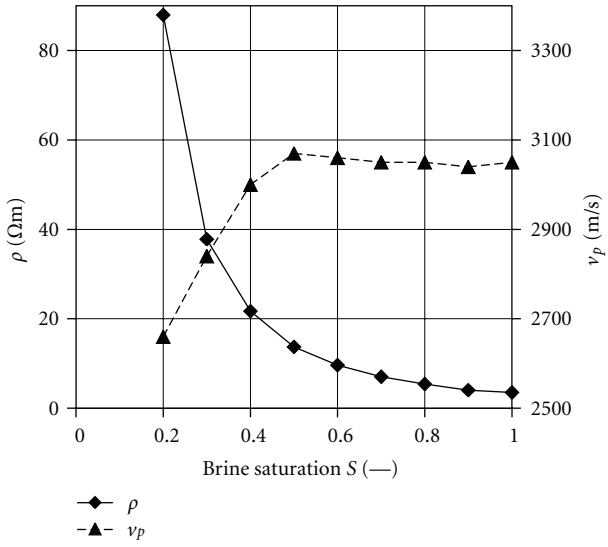

Figure 1: Experimental P-wave velocity (v_p) and electrical resistivity (ρ) of sandstone reservoir versus brine saturation (S) showing ρ far more sensitive to S than v_p [4].

and risk analysis). It aims at studying long-term CO_2 attenuation and migration in deep and shallow layers (including saline and fresh water aquifers), along with assessing storage capacity and analyzing risk. Various synthetic, almost realistic, storage scenarios are simulated for formations of the North German Basin that seem suitable for CO_2 storage. Our main task is to develop optimized, constrained monitoring strategy techniques for CCS using a combined seismic and ERT approach. This approach focuses on (1) developing a constrained electrical resistivity-modeling strategy based on a priori subsurface knowledge from seismic time-lapse imaging (some years) and logging data, and (2) reliably inverting continuous ERT time-lapse imaging to yield spatiotemporal developments in the intrinsic physicochemical properties of CO_2 reservoirs and cap rocks with time.

1.1. Optimized and Reliable Borehole ERT. Inverse ERT algorithms, however, tend to smear resistivity values from any given voxel to adjacent voxels (e.g., [8]). Based on the sensitivity functions, ERT in boreholes performs near the electrodes (boreholes) better than in the interwell region. Electrical sensitivity is used to select an array for a certain target but one that does not necessarily has the best possible resolution. Thus, a new approach of array optimization was recently developed to search for electrode configurations that maximize survey resolution (e.g., [9]). The optimization algorithms take into account the trade-off between the spatial and temporal (measurement time) resolution. They select measurements based on the contribution to the cumulative sensitivity of the array (e.g., [10]) or the model resolution matrix, R (e.g., [11]). R depends on sensitivities of all configurations plus regularization types used in the inversion [12]. For an arbitrary electrode array, the algorithms generate optimized (opt) data sets that have far less size than the comprehensive one and almost the same resolution of the targets. This comprehensive set includes all possible viable electrode configurations conducted within this array and possesses the maximum possible resolution, see next sections. The application of this 2D array optimization was recently extended into borehole-borehole and surface-borehole surveys [13–15]. The last algorithm is applied here. This algorithm strongly improves the ERT resolution in the interwell region (commonly low) to approach the resolution of the highly sensitive region close the boreholes.

The sensitivity accounts only for data sampling and model heterogeneities. As an alternative, the region of investigation index (ROI) is used to assess the whole 2D inversion procedure such as the data sampling and noise, model discretization and regularization, and nonlinearity [16, 17]. Thus, the reliability of ERT 2D tomograms will be evaluated here by ROI in addition to the relative model difference (residual) between each input and inverted output model.

For ERT in borehole surveys, the topographical aspect ratio (AR) is defined by the vertical length of the electrode array divided by the horizontal crosshole offset. Thus, resolution is enhanced by increasing the density (i.e., number and thus costs) of expensive monitoring wells in the area of plume migration. Newmark et al. [18] studied AR values of 2, 1.5, and 1 and found that they (in this order) show the best, intermediate, and worst resolution, respectively. In this study the lower boundary of AR is extended down to 0.25 which leads to a further decrease in the number (and thus costs) of monitoring wells. A broad AR range (0.25–2) is tested to determine its optimum value between the highest and lowest resolution (of AR = 2 and 0.25, resp.) that corresponds to the highest and lowest number of monitoring wells (i.e., costs), respectively.

1.2. Problem and Objectives. Until now ERT is rarely applied for the CCS problematic in deep saline reservoirs. Only few recent studies partly treated this problem, for example, feasibility studies by Christensen et al. [19] and sensitivity investigations for some specified CO_2 plume forms using point and long (metal-cased) borehole electrodes by Ramirez et al. [20]. Also there is a deficit of field sites for CO_2 sequestration that are equipped by adequate acquisition infrastructures for ERT surveys. All these lead to a strong demand for systematic ERT modeling investigations. In this study, extensive, systematic numerical ERT 2.5D modeling is carried out, and the results are analyzed for different virtual scenarios of injected wedge-like CO_2 plumes (dimensions, S_{CO_2} or ρ) as a function of electrode configuration, burial depth, AR, data noise, and setup parameters of modeling constraints (mainly regularization parameters, see next sections). Moreover, ROI analyses and residuals are applied to evaluate the resolving capability of various electrode configurations and inversion procedures. The technique's robustness in the field is tested by adding three different random errors to data sets. These studies aim to test the capability of (non-)standard and optimized ERT techniques (partly developed here) to resolve the subsurface CO_2 storage targets as a function of diverse parameters related to hydro-/geologic and geochemical subsurface properties (mainly of saline reservoir and cap rock),

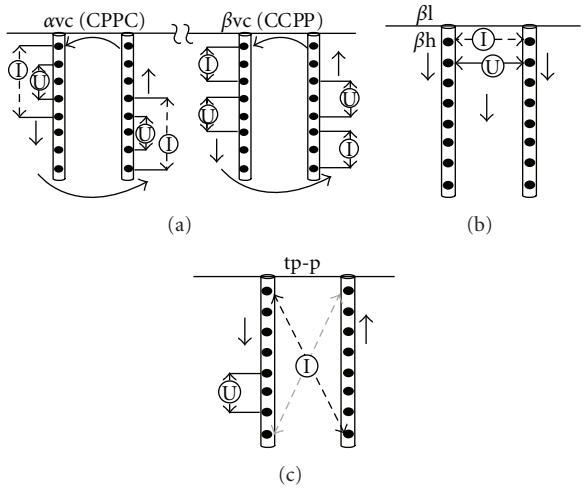

Figure 2: Tripotential electrode configurations α and β applied for electric resistivity tomography in boreholes (inhole and crosshole) using 4-pole of current (C) and potential (P) electrode pairs. The survey can be conducted in circulating (c) vertical, v (a), lateral, l and horizontal, h (b) modes and tripole-pole, tp-p (c) which is a special type of circulating vertical configuration with fixed C electrodes [24].

CO_2 plume, survey design, data acquisition, and modeling techniques.

In the next sections, I describe the applied borehole electrode configurations, the experiment setup of the subsurface model scenarios, and modeling varieties. I then discuss, summarize, and conclude the results of the different numerical simulations. Optimization algorithms, noises, depth effect, and modeling constraints are not shown here. They are contained in Hagrey [2, 14, 15] and Hagrey and Petersen [21].

2. Borehole Electrode Configurations

Similar to surface surveys, ERT data acquisition between two borehole electrode arrays can be conducted in the tripotential 4-pole configurations α (CPPC, C = current electrode, P = potential electrode), β (CCPP) and γ (CPCP), and their reciprocals. The γ configurations can be derived from α and β measurements, that is, they are not independent and are usually excluded from the data [22]. The rest of α and β measurements are accomplished in vertical (v, at 90°), horizontal (h, 0°), and lateral (l, >0–<90°) modes (Figure 2). These 4-pole modes are carried out within the same borehole (inhole) or distributed between the two boreholes (crosshole). Table 1 shows all possible configurations α and β for the inhole and crosshole modes [23]. Each configuration consists of two inhole and three crosshole arrangements.

For an array of N electrodes, the whole comprehensive data set contains $[N(N-1)(N-2)(N-3)/8]$ independent nonreciprocal 4-pole configurations (Table 2, [25]). Excluding the less stable inversion configurations from this whole set results in a more effective data set, simply called here comprehensive data set. These redundant configurations include γ configurations and those with geometric factors larger than that produced by the dipole-dipole array where the maximum dipole separation is 6a (a = electrode spacing, Figure 2). The comprehensive data set with all viable configurations should provide the best possible resolution [26]. It contains all subsurface information that can be gathered by an N-electrode array. Table 2 displays the size of the whole and effective comprehensive data sets in comparison with the standard ones for a collinear 32 electrode array and circulating arrays between two boreholes, each of 16 electrodes. The effective comprehensive set in boreholes contains more than 80,000 data points and is even about 0.65 of its whole set but more than 450 times each of the standard dipole-dipole and Wenner sets. This justifies applying the new approach of electrode optimization to generate optimized data sets of far lower size and almost the same resolution as the comprehensive ones, that is, of highly spatiotemporal resolution (for more details, see [14, 15]). Briefly this opt array improves the ERT resolution particularly in the interwell region which is commonly low compared to that of the region close the boreholes.

Ten different borehole surveys of standard, nonstandard, and optimized configurations are investigated here (Table 3, Figure 2). The vertical (v) circulating (c) configurations αvc and βvc represent the comprehensive data sets with all possible α and β electrode combinations, respectively. Their corresponding subconfigurations αvcs (s = symmetrical around the midpoint) and βvcs include only the conventional symmetrical arrangements of Wenner and Schlumberger, and dipole-dipole, respectively. The configurations βl and βh represent lateral (l) and horizontal (h) bipole-bipole configurations, where their C- and P-pairs are split between the two boreholes (CP-CP). The configuration βl represents the comprehensive data set acquired in all possible electrode combinations and orientations of this bipole-bipole (CP-CP) arrangement. Its subset βh is conducted with horizontal current electrodes (flows) only.

The tripole-pole (tp-p) is a special type of vertical circulating crosshole configurations [24]. It has fixed C electrodes (the respective upper- and lowermost electrode of the first and second hole, and vice versa; Figure 2) and moving P electrodes between any other possible combinations of electrode pairs in each borehole separately (i.e., CPP-C, C-PPC, PPC-C, and C-CPP of Table 1). It shows near-vertical current flows that are strongly influenced by horizontal layers in the interwell region. As opposed to tp-p, bipole-bipole configurations (βl and βh) have mostly lateral current flows, that is, a low resolution for horizontal structures, but detect better vertical structures. The new complex data sets βhtp (sum of βh and tp-p) and $\alpha\beta$vcs (sum of αvcs and βvcs) are introduced for the first time in this study. Each should reflect the advantages of its constituting arrays. Their combined current flows and potential measurements in various possible combinations and directions should be able to resolve targets of varying orientations. The applied opt data set (3000 data points) is less than 4% of the comprehensive set but has an average relative resolution of 0.96% (Table 3).

Table 1: All possible 4-pole tripotential configurations α and β (nonequivalent, nonreciprocal) of a survey between two borehole electrode arrays.

Configure	Group				
	Inhole			Crosshole	
	4-0	0-4	3-1	1-3	2-2
α	CPPC-0	0-CPPC	CPP-C	C-PPC	CP-PC
β	CCPP-0	0-CCPP	CCP-P	C-CPP	CC-PP

For example, group 4-0 denotes for number of electrodes (current, C/potential, P) in the first (4) and second (0) boreholes, respectively.

Table 2: Data set size of 4-pole configurations for a collinear N (32) electrode array and circulating crosshole array of 16 electrodes in each borehole.

Data set	Relation	Collinear ($N = 32$)	Circulating crosshole array ($N = 16 \leftrightarrow 16$)
Comprehensive, whole (independent, nonreciprocals)	$N(N-1)(N-2)(N-3)/8$ ($\alpha + \beta + \gamma$) data	107,880	122,760
Comprehensive, effective (whole compreh.—redundant)	($\alpha + \beta$) data (no γ + no noisy)	68,621	80,738
Dipole-dipole β ($\mathfrak{a} = 1$, n = 1–6)	$((N-3) + (N-8)) \times 3$	159	165
Wenner, α (CPPC)	$(N-1)(N-2)/6$	155	165

Redundant data include configurations of γ and noisy data of very low voltage.
Noisy data are those with geometric factor larger than that of dipole-dipole configuration of maximum dipole factor of 6.

Table 3: Applied configurations for two vertical arrays, each of 16 electrodes (see Figure 2). The corresponding electrodes in each borehole are set at equal depths with unit interval.

Configuration	Data no.	Characteristics
(1) tp-p	813	Vertical current flow, horizontal resolution
(2) βh	1,240	Horizontal/lateral current flow, better data quality, better vertical (less lateral) resolution
(3) βl	14,440	
(4) βhtp	2,053	Sum of βh and tp-p ((1) + (2))
(5) αvcs	1,796	Sum of Wenner and Schlumberger
(6) βvcs	1,177	Dipole-dipole
(7) $\alpha\beta$vcs	2,973	Sum of αvcs and βvcs ((5) + (6))
(8) αvc	34,788	Comprehensive including nonstandard and standard (αvcs and βvcs in αvc and βvc, resp.) configurations
(9) βvc	31,510	
(10) opt	3,000	Optimized data set with less than 4% size but 97% resolution relative to that of comprehensive set

c: circulating, v: vertical, α, β: tripotential configuration, l: lateral, s: symmetrical, tp-p: tripole-pole, h: horizontal, opt: optimized.

3. Subsurface Model Scenarios

To keep the virtual CO_2 sequestration modeling more realistic, the formation parameters of the starting subsurface scenarios used to generate the synthetic data have been taken from published data, for example, CO_2 SINK test site of Ketzin, near Berlin (e.g., [5, 27, 28]). The applied single subsurface models consist of the electrically almost insulating, supercritical CO_2 plume ($\rho_{CO_2} \approx \infty$) sequestrated at the top of a conductive saline sandstone reservoir ($\rho_{\text{reservoir}} = 3\,\Omega\text{m}$, $\rho_{\text{brine}} = 0.20\,\Omega\text{m}$, salinity 35–55 g/L, Φ = 20–25%), (Figure 3). This reservoir is capped by an impermeable siltstone ($\rho = 8\,\Omega\text{m}$ with varying thicknesses in the range $2\mathfrak{a}-9.5\mathfrak{a}$ ($\mathfrak{a}$ = electrode spacing)) to prevent upward CO_2 leakages. Model dimensions in this study are given in unit of $\mathfrak{a}$ which is often assumed to be 1 m. The CO_2 plume is simulated by the common wedge shape with bulk resistivities, ρ_{plume} of 100, 30, 15, and 10 Ωm (corresponding to saturations, S_{CO_2} of 80, 60, 40, and 30%, resp., as calculated from (2), and varying thicknesses (0.5$\mathfrak{a}$–13$\mathfrak{a}$) and widths (0.5$\mathfrak{a}$–13$\mathfrak{a}$)) [29].

4. Applied Procedures

The 2.5D forward and inverse ERT modeling of deep CO_2 plume was carried out using new codes based on algorithms for shallow surveys (e.g., [30]). All codes use the half-space solution with a fine mesh grid to accurately model the whole region. The Neumann and mixed boundary conditions are used for the top surface and the side/bottom boundaries, respectively. The program optimizes automatically a

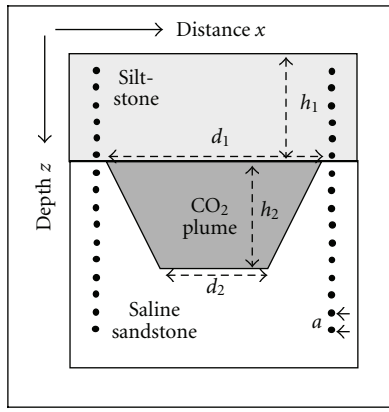

Model	d_1	d_2	h_1	h_2
W_1	13	0.5	2	3.5
W_2	13	2	3.5	11.5
W_3	13	3	4.5	10.5
W_4	13	4	5.5	9.5
W_{41}	13	6	5.5	7.5
W_{42}	13	8	5.5	5.5
W_5	13	10	7.5	3.5
W_6	13	12	9.5	1.5
W_7	13	12.5	9.5	1
W_8	13	13	9.5	0.5

Figure 3: Subsurface model scenarios of saline sandstone reservoir (resistivity, $\rho = 3\,\Omega$m) with CO_2 wedge-like plume of varying width (d), thickness (h), depth and saturation (80, 60, 40, and 30%, i.e., $\rho = 100$, 30, 15, and 10 Ωm, resp.) capped by siltstone (8 Ωm) together with borehole electrode arrays (•) used in the survey. d_1, d_2, h_1, h_2 are given in units of electrode spacing a.

sufficient number of additional mesh grids far from the electrodes (5a–10a) at these side/bottom boundaries.

An extensive numerical investigation was started by generating synthetic data sets of apparent resistivity (ρ_a) from 2.5D forward simulation as a function of (1) ten wedge-like models (Figure 2), (2) four S_{CO_2} values, (3) ten electrode configurations (Table 3, Figure 1), (4) seven ARs, (5) two burial depths (1a and 101a) and (6) three noise levels (1%, 3%, and 5%). This forward modeling has resulted in more than 8000 synthetic data sets for these diverse model scenarios with and without the wedge-like CO_2 plume. Each synthetic data set was filtered to remove any outliers and any ρ_a values of high geometric factor which may cause a potential leakage. The filter ensures also the absence of any equivalent, reciprocal, or γ configurations from the data set. Each filtered data set has been inverted independently eight times using different setup constraint parameters. This results in more than 100,000 tomograms for all applied synthetic data sets. The diverse setup constraints applied in the inversion mainly include regularizations with the minimization methods of least squares (L_2) or robust blocky normalization (L_1), and initial models of a constant homogeneous resistivity or an approximate inverse model.

The reliability of the forward modeling using finite-element method (with the more accurate trapezoidal elements instead of triangle ones) was confirmed before starting inversions using a homogeneous medium with a constant resistivity. Compared with this constant resistivity, the resulting deviations of the single apparent resistivities (ρ_a) for each applied synthetic data set generally do not exceed 3%. These deviations are similar to the normal error level in the real data and are considered here as a noise in the synthetic data sets.

Among the 10 examined wedge-like scenarios, this study focuses mainly on models W_1, W_{42}, and W_8 with the largest (13a), intermediate (5.5a), and least (0.5a) thicknesses for the CO_2 plume (Figure 3). The electrode coverage for the cap rock is least for W_1 (only 1a), intermediate for W_{42} (5a), and best for W_8 (11a). These CO_2 storage scenarios represent examples with optimum target dimensions (W_{42}) and problems of thin layers (plume in W_8 and reservoir below the plume in W_1) and thin widths (lowermost triangle apex in W_1). Among the eight independent inversions for each data set, only the one with the best-fitting model (least root mean square error, rms-error) is considered for further studies.

In the following, any inverted tomogram with its single target anomalies (CO_2 plume, host reservoir rock, and cap rock) is evaluated relative to the starting input model according to the following criteria:

(1) the reconstructed geometry, shape, and position,

(2) the recovered resistivity magnitude,

(3) the sharpness of the boundaries.

5. Results and Discussions

In the following, the reconstructed ERT tomograms for W_1, W_{42}, and W_8 scenarios will be described and discussed only as a function of the applied CO_2 plume scenarios (dimensions, S_{CO_2} or ρ), electrode configurations, ARs and noises.

The overall average rms-error for all inverted data sets approaches 0.9% with a nearly similar distribution between tomograms inverted by the robust L_1 norm and their corresponding models of the L_2 norm. For all studied data sets, every best-fitting tomogram (least rms-error almost of <0.5% and average iteration number of 5), among its independent eight inversions, was optimized with the L_1 norm. This low rms-error value is explained by the good convergence of the synthetic data sets toward the final solution. The average rms-error values are least for the lateral/horizontal configurations (βl/βh), intermediate for the opt and vertical circulating symmetrical configurations (αvcs, βvcs, $\alpha\beta$vcs), and highest for the comprehensive (αvc, βvc), tp-p and βhtp. One may note that the misfit distribution in these arrays is directly proportional to the data number with singularity problems and/or high geometric factors (i.e., of voltage leakages).

In all studied cases, the L_1 tomograms always show sharper boundaries and better magnitude recovery for the single

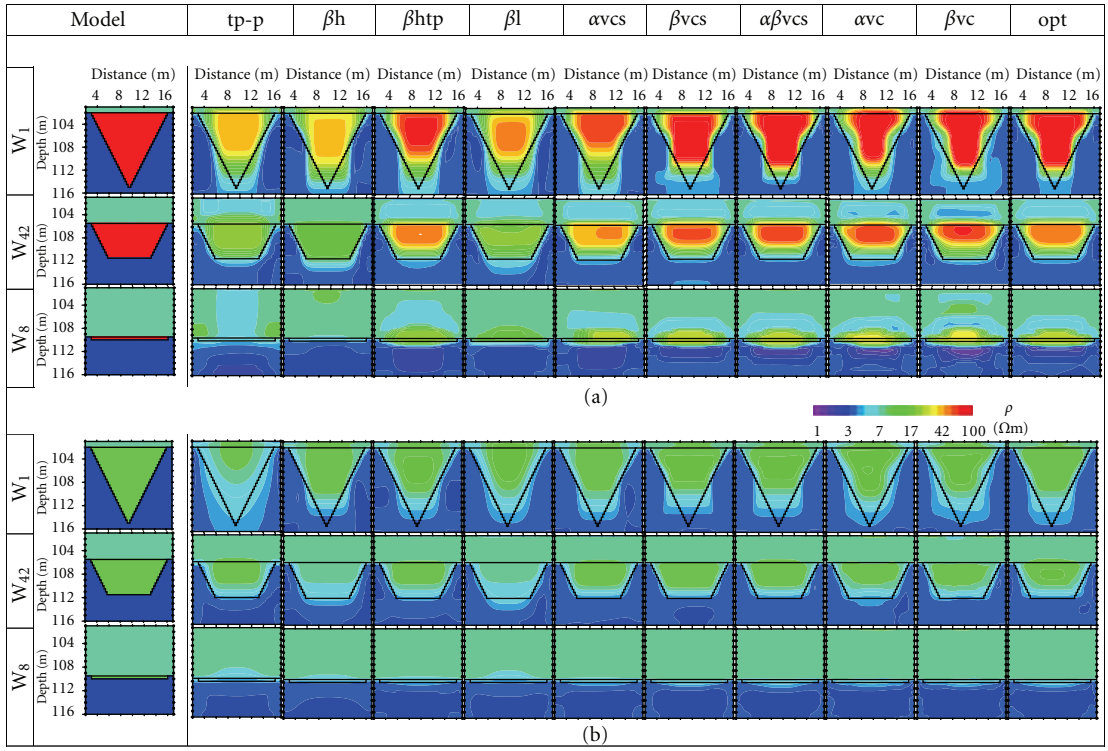

FIGURE 4: Numerical resistivity tomograms (3rd–12th column) inverted for different wedge-like CO_2 plumes (W_1, W_{42}, W_8, 1st-2nd column, see Figure 3) of varying saturations—resistivity of 100 (a) and 10 Ωm (b)—and 4-pole electrode configurations (1st row, see Figure 2 and Table 3 for symbols) between two borehole electrode arrays (•). All models show root mean square errors of less than 1%. Solid lines refer to target boundaries.

targets than the L_2 tomograms, that is, L_1 inversion fits better for resolving sequestration targets with sharp boundaries. These results are in accordance with the evidence that the L_1 norm tends to produce models that are piecewise constant, whereas the L_2 norm tends to smear out the sharp boundaries [19].

Briefly every best resolved output tomogram (among its eight independent inversions) resulted from the set of inversion constraint parameters which incorporates the use of (1) accurate calculation options at the expense of computation time (e.g., the standard Gauss-Newton algorithm to (re-)calculate the Jacobian matrix and optimization, 4 nodes per a and mesh grid to reduce singularity errors, the model refinement of half width and crosshole model of half size, etc.), (2) a robust blocky L_1 norm for sharp boundaries instead of smooth L_2 norm for gradual changes, (3) sufficient boundary meshes (>5a), and (4) low damping parameters for these synthetic data (almost noise free). Based on these discussions, all (best-fitting) tomograms considered throughout the next sections were inverted using the robust L_1 norm.

6. Effect of Configurations and Model Scenarios

Figure 4 shows examples of the reconstructed 2D tomograms (with the best-fitting least rms-error) for the subsurface scenarios W_1, W_{42}, and W_8 of different CO_2 plume dimensions and only the two extreme S_{CO_2} of 80 and 30 g/L (corresponding ρ of 100 and 10 Ωm, resp., Figure 3). These scenarios are situated at a depth of 101a (to the uppermost electrode). They are reconstructed for the applied 10 electrode configurations (Table 3, Figure 2) using the aspect ratio (AR) of 1.

In most applied cases, the resistive wedge-like CO_2 plume together with the conductive saline reservoir of hosting sandstone and the impermeable siltstone cap rock are generally mapped directly by the inverted absolute ρ tomograms (no model differencing between tomograms with and without plume). Most configurations generally reconstruct these three targets with varying degrees of smearing and artifacts. This smearing is reflected on the single tomograms by target anomalies of lower magnitude, larger volume, and blurred boundary relative to that of their input models. This smearing is evaluated quantitatively by the ROI and residual analyses, see next section. The mapping capability generally decreases with decreasing dimensions (thickness, width) and resistivity of the targets. With the exception of the lateral/horizontal (βl/βh), all other configurations can reconstruct even the worst CO_2 plume scenario (of the least thickness of W_8 and resistivity of 10 Ωm). Based on the previously mentioned criteria for evaluating the inverted tomogram anomalies (geometry, position, ρ amplitude, and boundary sharpness), the mapping capability generally is better for configurations with multiply orientated current flows and potential measurements (αvc and βvc, their subsets αvcs, βvcs, and $\alpha\beta$vcs, as well as opt and βhtp) than those of

only lateral (βl), horizontal (βh), and vertical (tp-p) current injection. Tomographic anomalies of the later configurations generally show lower ρ magnitude than that of the former configurations, that is, configurations βl, βh and tp-p underestimate the ρ magnitude compared with the input models, see next section.

Among the applied scenarios, the mapping capability for the sequestration targets (cap rock, plume, and reservoir) is best for W_{42}, intermediate for W_1, and least for W_8. Tomogram W_1 shows strong smearing effects for the lowermost apex of plume triangle and the cap rock with their surroundings. Both targets have the thin layer problem with electrode coverage of ≤ 1 which causes this smearing governed by the equivalence principle (e.g., [15]). For a thin resistive CO_2 plume target, the inversion code is not able to resolve thickness and resistivity parameters of certain resistive model features individually but only their product (resistance). The horizontal boundaries of the upper reservoir/plume and lower plume in W_{42} and partly W_1 are generally resolved slightly better than the inclined boundaries of the plume.

Regarding the applied configurations, the vertical circulating αvc and αvcs generally resolve inclined boundaries better than their corresponding βvc and βvcs. This may explain the occasional moderate resolution of $\alpha\beta$vcs tomograms (containing βvcs data) for the lower triangle apex of the plume in W_1. It is clear that the individual complex configurations βhtp (sum of βh and tp-p) and $\alpha\beta$vcs (sum of αvcs and βvcs) combine the features (mostly of better resolution) of their corresponding single constituents. Each complex configuration contains more data measured in more orientations and thus carries more information than its constituent data sets (cf. [31]). On the other hand, models of the vertical circulating β (βvc and βvcs) tomograms generally reflect higher (better) resistivity magnitudes of the targets than their corresponding α (αvc and αvcs) models. The resistivity magnitude approaches its real value in the target centre and deviates increasingly from this with distance toward the contact with the next target. As opposed to real data, the inversion models do not show the usual poor resolution with strong artifacts around the boreholes. These are due to the heterogeneities caused by boring and electrode installation and/or the distorting effects of the conductive borehole fluid relative to the resistive host rock [32].

Regarding the data set size, the resolution of opt tomograms (nearly 3,000 data points) is almost similar to the best possible resolution of each of the comprehensive αvc and βvc models (each of >30,000 points) and far better than that of βl tomograms (14,440). Obviously, the resolution for the noncomprehensive data sets is best for opt, above moderate for the complex $\alpha\beta$vcs and βhtp, moderate for αvcs and βvcs, and least for βh and tp-p.

Briefly, the lateral/horizontal configurations (βl and βh) are more robust against measurement errors due to current and voltage leakages. In these configurations, splitting the current and potential electrode pair between boreholes (i.e., CP-CP) maximizes the measured voltage (e.g., [23]). Large borehole offset (i.e., P_1-P_2 distance), however, may include the telluric noise in the data (e.g., [33]). This noise can be minimized by periodically reversing the current flow in the current electrodes. These arrays result in poorly resolved anomalies, especially for lateral boundaries, often with underestimated ρ magnitudes. This is due to the predominance of current flows and potential measurements in the lateral directions with poor data coverage in the vertical one. Configurations having either a C or P electrode pair or both in the same borehole (inhole) such as most of the vertical circulating α and β (αvc, βvc, αvcs, and βvcs, Table 1) configurations have the singularity problem of very low voltages. However, their filtered data sets after removing this noise can resolve well the subsurface targets of CO_2 plume, reservoir, and cap rock assuming enough coverage of more than one electrode spacing. These conclusions are in accordance with that of, for example, Oldenburg and Li [16] and Oldenborger et al. [34] and opposed to that of Zhou and Greenhalgh [23]. In solute transport experiments, the former authors found that the vertical βvcs tomograms show more reliable subsurface structures than the horizontal β tomograms. Bing and Greenhalgh stated that the acquisition data for vertical inhole configurations are easily obscured by background noise and yield images inferior to those from lateral/horizontal configurations βl and βh.

7. Evaluation of Reconstructed Tomograms

This evaluation is carried out by the ROI analysis and the model difference (residual) relative to the input model. The ROI analysis is started by conducting two independent inversions of the same dataset using different resistivity values (q_A and q_b) for homogeneous reference models. Values of q_A and q_b are calculated from the average logarithmic ρ_a using two different multiplication factors. The inversion results from these two starting models are used to calculate the ROI value for each pixel, defined as [35]:

$$\mathrm{ROI}(x,z) = \left[q_A(x,z) - q_B(x,z)\right]\left(q_A - q_B\right)^{-1}. \quad (3)$$

The ROI approaches zero when the model is well constrained by the data (the two inversions reproduce very similar ρ values) and one when the model has a very poor data coverage. The two inversions of each ROI analysis were conducted using the same set of inversion setup parameters (resulted in the best fitting tomograms, see before) and only three iterations. Higher iteration numbers were tested and resulted in artifacts as the algorithm tries to reduce the data misfit by modeling the noise as well. Different pairs of multiplication factors (0.1 and 10, 0.1 and 10, and 0.2 and 5) were applied here and yield similar results (see also [34, 36]).

On the other hand, the relative resistivity difference or residual ($\Delta\rho$) between each corresponding pixel of the input (ρ_{input}) and output (ρ_{output}) 2D models is calculated by

$$\Delta\rho = \left(\rho_{\mathrm{output}} - \rho_{\mathrm{input}}\right)\left(\rho_{\mathrm{output}} + \rho_{\mathrm{input}}\right)^{-1}. \quad (4)$$

Moreover, a random noise at 1, 2, and 5% levels was added to the synthetic data sets, in addition to their forward modeling errors (up to 3%), to evaluate noisy field effects on the inversion. Adding noise in this order generally increases

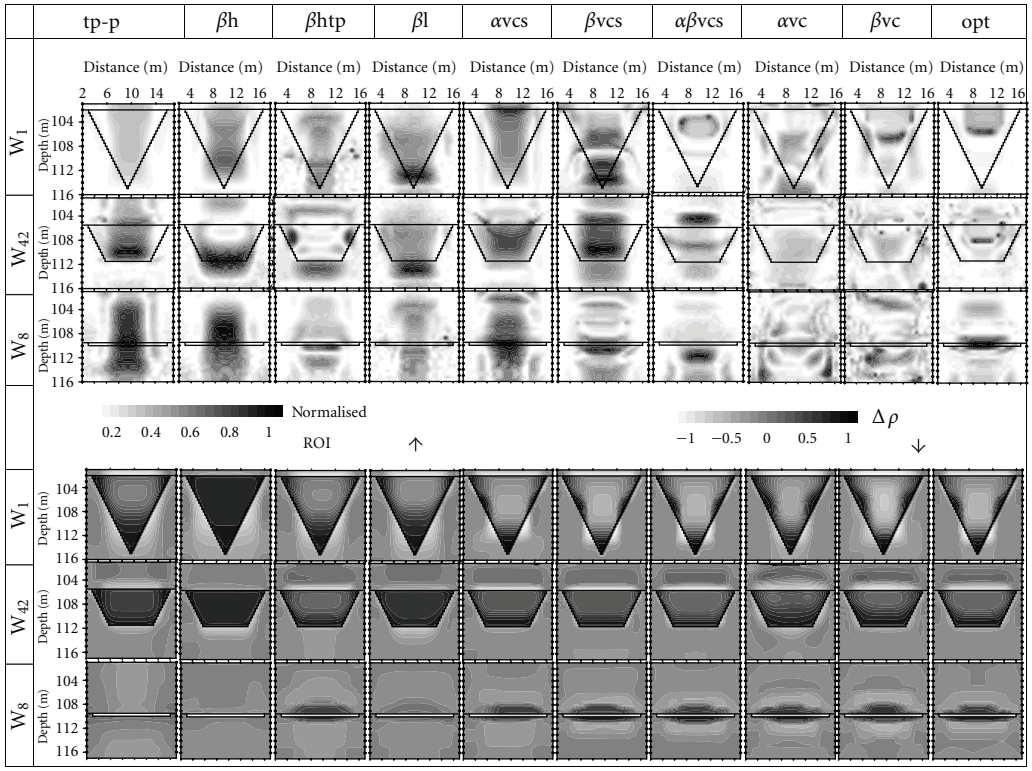

Figure 5: Evaluation of the reconstructed electrical resistivity tomograms (depth of 101a, a = electrode spacing) using methods of region of index, ROI (top, (3)) and relative model difference, $\Delta\rho$ (bottom, (4)) for survey between two borehole electrode arrays (•) as a function of subsurface scenario (W_1, W_{24}, and W_8, 1st column), and electrode configuration (see Table 3 for symbols). Solid lines refer to target boundaries.

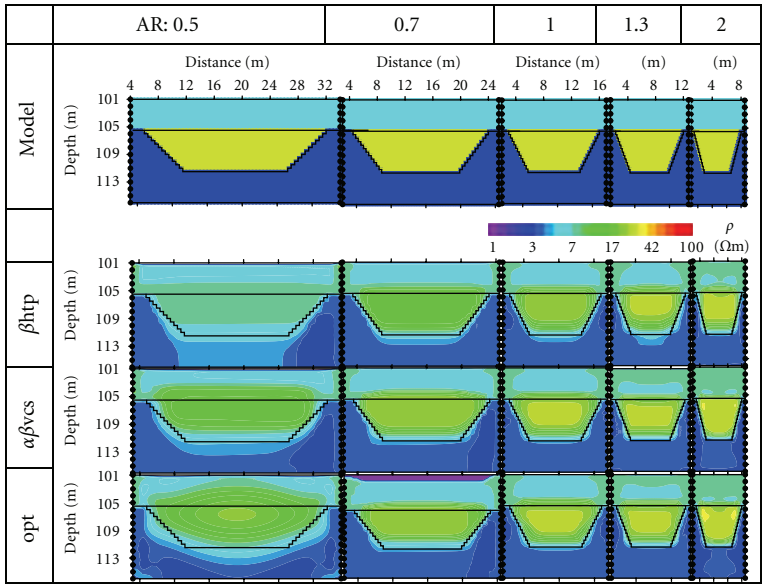

Figure 6: Effect of aspect ratios, AR (first row) on ERT tomograms, resulting from wedge-like CO_2 plume scenario W_{42} (Figure 3, second row) with 30 Ωm plume resistivity for 4-pole configurations βhtp, $\alpha\beta$vcs and opt (see Figure 2 and Table 3 for symbols) between two borehole electrode arrays (•). All models show root mean square errors of less than 1%. Solid lines refer to target boundaries.

the rms-error values by a factor of 2 to 9 but slightly decreases the mapping capability, particularly for W_1 and W_{42}. Ramirez et al. [20] obtained similar results; the effect of the random error is insignificant for anomalies of a large size and magnitude.

Figure 5 shows examples of the resulting ROI and $\Delta\rho$ tomograms as a function of the applied electrode configurations carried out for the subsurface scenarios W_1, W_{42}, and W_8 at 101a depth only. Constraining of inverted tomograms by data coverage is best (lowest values for ROI and partly $\Delta\rho$) for the comprehensive αvc and βvc, and opt arrays, intermediate for the complex $\alpha\beta$vcs and βhtp, and poor (highest ROI values) for the others. This confirms the effectiveness of our optimization approach applied here to generate a practical opt dataset of high resolution.

Unlike real field data, this synthetic modeling analysis does not show the usual disadvantageous low resolution of high values of ROI and $\Delta\rho$ (of bad data and thus resolution) around the boreholes due to the heterogeneities resulting from boring and electrode installation. The highest values of ROI and $\Delta\rho$ with the least data coverage and resolution are concentrated in the central interwell region which is a common disadvantage for ERT results. Also ROI and $\Delta\rho$ analyses reflect similar results between the corresponding single tomograms of shallow (1a depth, not shown here) and deep scenarios (101a depth). This similarity reflects the reliability of the applied techniques. A comparison with published results (e.g., [34]) shows that the vertical configurations reflect better resolution (of lower ROI values) than the lateral ones which confirms the results obtained here.

Briefly, tomograms of $\Delta\rho$ and ROI generally show similar results regarding the mapping capability of the single applied arrays. They reflect well the common smearing effects of varying degrees. These effects lead to overpredicted volumes, underpredicted magnitudes, and blur boundaries of the target anomalies. This study shows clearly that the complex (βhtp and $\alpha\beta$vcs) arrays with multiply oriented measurements in addition to opt arrays with practical data sizes are recommended for highly spatiotemporal resolution and will be considered further in this study.

8. Effect of Tomographic Aspect Ratio (AR)

Extensive tests for seven different AR steps within 0.25–2.0 range were performed as a function of the applied subsurface scenarios (Figure 2), S_{CO_2}, burial depths, electrode configurations (Figure 1, Table 3), noises, and modeling setup parameters. At the AR values (0.5, 0.7, 1.0, 1.3 and 2), Figure 6 shows some best-fitting (least rms-error) tomograms resulting from unconstrained inversions only for the highly resolving arrays (βhtp, $\alpha\beta$vcs and opt) and the subsurface scenario W_{42} with S_{CO_2} of 60% ($\rho_{CO2} = 30\,\Omega$m).

Figure 6 shows that the obtained mapping capability (including resolution) generally increases with increasing AR from 0.5 to 2. This occurs although the lateral boundaries of the CO_2 wedge plume become more vertical with increasing AR. This mapping improvement with increasing AR is also associated with a slight increase of the recovered ρ magnitude of the CO_2 plume relative to that of the starting input model. Most other results of the previous sections are manifested here such as the poor mapping resolution of thin layers (of W_1 and W_8 scenarios, not shown here). At AR = 1, the lowermost triangle apex of W_1 is predominated either from the reservoir anomaly or from a wide smeared zone of the plume. At AR > 1, the apex resolution increases with increasing AR and approaches best results at AR of 2. Based on the applied electrode configurations, the resolution for tomograms of the vertical circulating and opt arrays is better than for those of lateral/horizontal βl/βh and partly tp-p and βhtp configurations (partly not shown here). Compared with W_1 and W_8, W_{42} models are generally better resolved due to the better coverage of their target. The ability to detect and often map the three sequestration targets (CO_2 plume, reservoir, and cap rock) by unconstrained inversions is still possible with AR values down to 0.5 for the most studied scenarios (even those with the worst scenario of least thickness and ρ). This result is superior to that of published studies (e.g., [18]). These authors applied ERT techniques for site characterization and process monitoring and determined a minimum AR with acceptable output resolution of 1. In comparison, the minimum AR value (0.5) currently obtained in this study can lead to a decrease of the number of the expensive monitoring wells and the costs by a factor of 4 (i.e., $n^{(1/AR)}$, n: well number for AR = 1). The reconstructed output tomograms for lower AR values (<0.5) achieve a satisfactory resolution only for constrained inversions with an a priori fixing of boundaries and/or resistivities of the targets. The resolution increases with increasing the number of constraints.

9. Summary and Conclusions

Electrical resistivity tomography (ERT) techniques in boreholes are powerful in monitoring intrinsic property changes for storing the resistive (supercritical) CO_2 in conductive saline reservoirs. In this study, the mapping capability of various ERT techniques is studied for diverse wedge-like CO_2 plumes in a deep saline aquifer capped by an impermeable rock. Extensive, systematic 2.5D modeling studies (>100,000 models) were performed to test the ERT sensitivity for a multitude of parameters related to the subsurface setting (hydrogeology and geochemistry of reservoir and cap rock), CO_2 plume reservoir, survey design, data acquisition, and modeling techniques. The new array optimization approach is applied to generate optimized data sets (opt) of only 4% of the comprehensive set but of almost similar resolution. Forward simulations were carried out to generate diverse synthetic data sets (>8000) as a function of plume scenarios (different dimensions and CO_2 saturations S_{CO_2} or resistivity, ρ), burial depths, electrode configurations, random noise, and aspect ratios (AR). The data quality (<3% noises) is confirmed by results of tests on a homogeneous model with constant ρ. This numerical study principally reveals the capability of ERT techniques to resolve the various deep subsurface scenarios with the CO_2 sequestration targets (plume, host reservoir, and cap rock). Most important results may be summarized as follows:

(1) Most applied ERT configurations can generally map the sequestration targets of sharp boundaries directly by the absolute ρ tomograms (no model differencing) using L_1 robust inversions. All models, however, reflect smeared anomalies of lower magnitude, larger area, and blurred boundary.

(2) Superior to published studies, the detection of CO_2 targets is possible even for the worst scenario of 0.5a thicknesses (a = unit electrode length), 30% S_{CO_2}, and 0.5 AR. At lower AR values (<0.5), a satisfactory resolution can result only from constrained inversions with an a priori fixing of boundaries and/or resistivities of targets.

(3) The developed opt and complex ($\alpha\beta$vcs, βhtp) arrays (nearly 3000 data points) are recommended for surveys of highly spatiotemporal resolution. Their resolution is the second best after the comprehensive vertical arrays (αvc and βvc, each of >30,000 data) and far better than the comprehensive lateral array (βl, 14,400 data). These arrays improve the common low resolution of the ERT technique in the interwell region by combining configurations with current flows and potential measurements in all possible orientations.

(4) Lateral arrays (βl and βh) are more robust against measurement noise; their synthetic data sets result in tomograms with the least rms-error misfit, but their real field data may include natural telluric noise at large borehole offset.

(5) Analyses of the region of index, ROI, and residual model difference relative to the input model show that inverted tomograms of comprehensive (αvc and βvc), opt, and complex ($\alpha\beta$vcs) configurations are better constrained by the data than those of the other applied ones. This tomogram reliability generally increases by increasing the data size.

(6) Sometimes the configuration tripole-pole (tp-p) is able to detect horizontal structures due to its near-vertical current flows. Contrary to this, lateral arrays (βl and βh) have lateral current flows and thus better resolution for vertical structures.

(7) The vertical circulating α and β data sets are collected partly with either or both of the current and potential electrode pair inhole and thus may show singularity problems. Filtering these data sets results in tomograms of better resolution than those of lateral arrays.

(8) Adding random noise (1%, 3%, and 5%) to the synthetic data (in addition to its forward modeling errors, up to 3%) increases the rms-error values (according to the error continuation law) by a factor of 2–9 but slightly decreases the mapping capability of the techniques, particularly for large targets.

10. Outlook and Recommendation

The current results give answers to some studied problems of 2D ERT mapping for CO_2 sequestration in deep saline aquifers. Many other problems related to the 2D/3D mapping and 4D monitoring are currently studied within the research activities of our MoPa project. These tasks include the following:

(i) Continuing the systematic 2.5D modeling studies for other CO_2 plume scenarios and extending these to 3D investigations with varying parameters related to modeling, data acquisition and methodology, geological setting and plume reservoir developments based on petrophysical approaches.

(ii) Applying approaches of time-lapse imaging for 4D monitoring of any CO_2 migration either laterally and downwards within the saline reservoir or upwards through probable postinjection fracturing of the cap rock caused by the high injection pressure. This includes monitoring of pre- and postinjection scenarios, developments of the new CO_2 reservoir, and any change in the porosity/permeability with time.

(iii) Risk analyses for any possible postinjection fracturing in the cap rock and upward CO_2 seepages into the near surface zone and especially freshwater aquifers.

(iv) Evaluating the spatiotemporal resolution of output tomograms using techniques of residual, 2D ROI, and 3D VOI. Quantitative analyses of ρ magnitude and spatial extension in the single pixels/voxels of the recovered tomograms with respect to the pre-injection model.

(v) Applying developed modeling techniques on more realistic subsurface scenarios by using available (meta)data of the North German Basin and ρ_a (hard data) inversion constrained by seismic and log information (soft data) to reduce the problems of nonuniqueness. Constrained inversion schemes should be able to fix resistivity regions and include boundaries in the output models.

(vi) Using petrophysical approaches to quantify inverted resistivity models in saturation, and the quality of the pore filler (brine and CO_2).

(vii) Refining and verifying the use of optimized configurations for enhancing the spatial resolution without a significant decline of temporal resolution.

(viii) Testing the developed techniques on real field data, for example, the sequestration site of Ketzin in collaboration with partners of the project CO_2 sink.

Acknowledgments

Special thanks to colleagues M. H. Loke for providing modeling programs, M. Strahser, W. Rabbel, and R. Meissner for critical comments, T. Wunderlich, S. Siebrands, and A. Ismaeil for MATLAB programs, and Associate Editor X. Yang and two anonymous reviewers for constructive recommendations. This study is funded by the German Federal Ministry of Education and Research (BMBF), EnBW Energie Baden-Württemberg AG, E.ON Energie AG, E.ON Gas Storage AG, RWE Dea AG, Vattenfall Europe Technology Research

GmbH, Wintershall Holding AG, and Stadtwerke Kiel AG as part of the CO_2-MoPa joint project in the framework of the Special Programme GEOTECHNOLOGIEN.

References

[1] M. Meadows, "Time-lapse seismic modeling and inversion of CO_2 saturation for storage and enhanced oil recovery," *Leading Edge*, vol. 27, no. 4, pp. 506–516, 2008.

[2] S. A. Hagrey, "First numerical ERT models for CO_2 plumes in saline reservoirs using crosshole configurations," in *Proceedings of the 1st EAGE CO2 Geological Storage Workshop*, p. 5, European Association of Geoscientists and Engineers, 2008.

[3] G. E. Archie, "The electrical resistivity log as an aid in determining some reservoir characteristics," *Transactions of the American Institute of Mining Engineers*, vol. 146, pp. 54–62, 1942.

[4] B. A. Kirkendall and J. J. Roberts, "Crosswell electromagnetic imaging, in advanced reservoir characterization in the Antelope shale to establish the viability of CO_2 enhanced oil recovery in California's Monterey formation siliceous shale," Annual Report DOE/BC/14938-12, National Petroleum Technology Office, 2003.

[5] A. Förster, B. Norden, K. Zinck-Jørgensen et al., "Baseline characterization of the CO_2SINK geological storage site at Ketzin, Germany," *Environmental Geosciences*, vol. 13, no. 3, pp. 145–161, 2006.

[6] A. L. Ramirez, J. J. Nitao, W. G. Hanley et al., "Stochastic inversion of electrical resistivity changes using a Markov Chain Monte Carlo approach," *Journal of Geophysical Research B: Solid Earth*, vol. 110, no. 2, pp. 1–18, 2005.

[7] J. Van Sijl, P. Winthaegen, B. Goes, and C. J. Peach, "Modelling ERT monitoring of CO_2-storage with enhanced coalbed methane recovery," in *Proceedings of the 69th European Association of Geoscientists and Engineers Conference and Exhibition*, pp. 1220–1224, London, UK, June 2007.

[8] F. D. Day-Lewis, K. Singha, and A. M. Binley, "Applying petrophysical models to radar travel time and electrical resistivity tomograms: resolution-dependent limitations," *Journal of Geophysical Research B: Solid Earth*, vol. 110, no. 8, Article ID B08206, pp. 1–17, 2005.

[9] P. Stummer, H. Maurer, and A. G. Green, "Experimental design: electrical resistivity data sets that provide optimum subsurface information," *Geophysics*, vol. 69, no. 1, pp. 120–139, 2004.

[10] T. Hennig, A. Weller, and M. Möller, "Object orientated focussing of geoelectrical multielectrode measurements," *Journal of Applied Geophysics*, vol. 65, no. 2, pp. 57–64, 2008.

[11] P. B. Wilkinson, P. I. Meldrum, J. E. Chambers, O. Kuras, and R. D. Ogilvy, "Improved strategies for the automatic selection of optimized sets of electrical resistivity tomography measurement configurations," *Geophysical Journal International*, vol. 167, no. 3, pp. 1119–1126, 2006.

[12] P. R. McGillivray and D. W. Oldenburg, "Methods for calculating Frechet derivatives and sensitivities for the non-linear inverse problem: a comparative study," *Geophysical Prospecting*, vol. 38, no. 5, pp. 499–524, 1990.

[13] I. Coscia, L. Marescot, H. Maurer, S. Greenhalgh, and A. G. Green, *Experimental Design for Cross Hole Electrical Resistivity Tomography Datasets*, EAGE Near Surface Geophysics, Cracow, Poland, 2008.

[14] S. A. Hagrey, *2D Optimisation of Electrode Arrays for Borehole Surveys*, EAGE Near Surface Geophysics, Dublin, Ireland, 2009.

[15] S. A. Hagrey, "2D optimized electrode arrays for borehole resistivity tomography and CO_2 sequestration modelling," *Pure and Applied Geophysics*. In press.

[16] D. W. Oldenburg and Y. Li, "Estimating depth of investigation in dc resistivity and IP surveys," *Geophysics*, vol. 64, no. 2, pp. 403–416, 1999.

[17] M. S. Zhdanov, *Geophysical Inverse Theory and Regularization Problems*, Elsevier, New York, NY, USA, 2002.

[18] R. L. Newmark, W. Daily, and A. Ramirez, "Electrical resistance tomography using steel cased boreholes as electrodes," in *Proceedings of the 69th Annual Meeting of Expanded Abstract*, p. 4, Society of Exploration Geophysicists, 1999.

[19] N. B. Christensen, D. Sherlock, and K. Dodds, "Monitoring CO_2 injection with cross-hole electrical resitivity tomography," *Exploration Geophysics*, vol. 37, no. 1, pp. 44–49, 2006.

[20] A. L. Ramirez, R. L. Newmark, and W. D. Daily, "Monitoring carbon dioxide floods using Electrical Resistance Tomography (ERT): sensitivity studies," *Journal of Environmental and Engineering Geophysics*, vol. 8, no. 3, pp. 187–208, 2003.

[21] S. A. Al Hagrey and T. Petersen, "Numerical and experimental mapping of small root zones using optimized surface and borehole resistivity tomography," *Geophysics*, vol. 76, no. 2, pp. G25–G35, 2011.

[22] E. W. Carpenter and G. M. Habberjam, "A tripotential method for resistivity prospecting," *Geophysics*, vol. 21, pp. 455–469, 1956.

[23] B. Zhou and S. A. Greenhalgh, "Cross-hole resistivity tomography using different electrode configurations," *Geophysical Prospecting*, vol. 48, no. 5, pp. 887–912, 2000.

[24] B. J. M. Goes and J. A. C. Meekes, "An effective electrode configuration for the detection of DNAPLs with electrical resistivity tomography," *Journal of Environmental and Engineering Geophysics*, vol. 9, no. 3, pp. 127–141, 2004.

[25] M. Noel and B. Xu, "Archaeological investigation by electrical resistivity tomography: a preliminary study," *Geophysical Journal International*, vol. 107, no. 1, pp. 95–102, 1991.

[26] M. H. Loke, F. A. Fouzan, and M. N. M. Nawawi, "Optimisation of electrode arrays used in 2D resistivity imaging surveys," in *Proceedings of the 19th Conference and Exhibition*, p. 5, Australian Society of Exploration Geophysicists, 2007.

[27] A. Ramirez, J. Friedmann, W. Foxall et al., "oint reconstructions of CO_2 plumes using a Markov Chain Monte Carlo approach," in *Proceedings of the 8th International Conference on Greenhouse Gas Control Technologies*, p. 6, Tondheim, Norway, 2006.

[28] D. Kiessling, C. Schmidt-Hattenberger, H. Schuett et al., "Geoelectrical methods for monitoring geological CO_2 storage: first results from cross-hole and surface-downhole measurements from the CO_2SINK test site at Ketzin (Germany)," *International Journal of Greenhouse Gas Control*, vol. 4, no. 5, pp. 816–826, 2010.

[29] E. Gasperikova and G. M. Hoversten, "Gravity monitoring of CO_2 movement during sequestration: model studies," *Geophysics*, vol. 73, no. 6, pp. WA105–WA112, 2008.

[30] M. H. Loke, I. Acworth, and T. Dahlin, "A comparison of smooth and blocky inversion methods in 2D electrical imaging surveys," *Exploration Geophysics*, vol. 34, pp. 182–187, 2003.

[31] A. Furman, T. P. A. Ferré, and G. L. Heath, "Spatial focusing of electrical resistivity surveys considering geologic and hydrologic layering," *Geophysics*, vol. 72, no. 2, pp. F65–F73, 2007.

[32] J. A. Doetsch, I. Coscia, S. Greenhalgh, N. Linde, A. Green, and T. Günther, "The borehole-fluid effect in electrical resistivity imaging," *Geophysics*, vol. 75, no. 4, pp. F107–F114, 2010.

[33] M. Blome, H. Maurer, and S. Greenhalgh, "Geoelectric experimental design—efficient acquisition and exploitation of complete pole-bipole data sets," *Geophysics*, vol. 76, no. 1, pp. F15–F26, 2011.

[34] G. A. Oldenborger, P. S. Routh, and M. D. Knoll, "Model reliability for 3D electrical resistivity tomography: application of the volume of investigation index to a time-lapse monitoring experiment," *Geophysics*, vol. 72, no. 4, pp. F167–F175, 2007.

[35] L. Marescot and M. H. Loke, "Using the depth of investigation index method in 2D resistivity imaging for civil engineering surveys," in *Proceedings of the Symposium on the Application of Geophysics to Engineering and Environmental Problems (SAGEEP '04)*, pp. F589–F595, Colorado Springs, Colo, USA, February 2004.

[36] J. E. Nyquist, J. S. Peake, and M. J. S. Roth, "Comparison of an optimized resistivity array with dipole-dipole soundings in karst terrain," *Geophysics*, vol. 72, no. 4, pp. F139–F144, 2007.